Principles of free-space optical microelectromechanical systems

R R A Syms
Optical and Semiconductor Devices Group, EEE Department, Imperial College London, Exhibition Road, London SW7 2BT, UK. email: r.syms@ic.ac.uk

The manuscript was received on 13 March 2007 and was accepted after revision for publication on 11 September 2007.

DOI: 10.1243/09544062JMES662

Abstract: Optical microelectromechanical systems (MEMS) combine miniature optical components with precision fixtures, elastic suspensions, and microactuators, and allow complex functionality at low cost. However, the effect of the bounded nature of the beams propagating through the system on design is profound. The current paper reviews the fundamental consequences. Using a Gaussian beam formulation, models of guided modes in gradient index media, bounded beams and imaging components are constructed. Propagation algorithms are described. The alignment tolerances for common component trains such as fibre-to-fibre and beam-to-fibre connections are derived, limits on the curvature of reflecting surfaces are established, the scaling laws of free-space optical MEMS are presented and the effect of beam size on filter performance is clarified. Examples such as variable optical attenuators, optical cross-connect switches, filters and tunable lasers are discussed.

Keywords: microelectromechanical systems, micro-opto-electromechanical systems

1 INTRODUCTION

Optical microelectromechanical systems (MEMS) have many applications in fibre telecommunications, since they combine complex optical functionality with high performance [**1**–**4**]. They often involve combinations of free space components such as mirrors, gratings, and lenses, and guided wave components such as fibres and lasers. Past reviews have concentrated on device technology. Here, instead, the underlying design principles are presented. In contrast to macroscopic systems, which can be understood using ray optics, optical MEMS involve either free-space propagation of bounded beams, or wave guidance, or a mixture of the two. Ray optics is therefore inappropriate, but simple designs can still be achieved by considering the properties of Gaussian beams, which propagate in free space and in cylindrically symmetric graded-index media [**5**, **6**]. Their properties lead to standard layouts, typically involving the expansion of a beam from a fibre to a size sufficient for effective interaction with a component such as a filter, followed by a reduction in size to allow coupling back into a fibre. Beam sizes can be controlled using lenses; however, there are clearly optimum arrangements, which should be identified to allow efficient packaging solutions [**7**]. Of course, real systems are imperfect. Any departures from ideal alignment, or in the components themselves, can lead to a reduction in throughput. The allowable insertion loss then determines the mechanical tolerances.

In section 2, the optical MEMS technology is reviewed, and in section 3, the essential theory of Gaussian modes is presented. In section 4, imaging components and general propagation algorithms are considered, and it is shown in section 5, how beam parameters are optimized. In section 6, alignment tolerances are considered, and in section 7, the effect of optical surface curvature. In sections 8, 9, 10, and 11, the principles of MEMS variable attenuators, switches, filters, and tunable lasers are described. Mechanical alignment issues are discussed and conclusions are drawn in section 12.

2 OPTICAL MEMS

Common methods of optical MEMS fabrication include anisotropic etching of single crystal silicon

[**8**], polysilicon surface micromachining [**9**], synchrotron lithography and electroplating (LIGA) [**10**], and deep reactive ion etching (DRIE) of bonded silicon-on insulator (BSOI) [**11**], as shown in Fig. 1. Three-dimensional structures may also be assembled by out-of-plane rotation [**12**]. Each method has its merits. Anisotropic etching allows precise formation of grooves and pits. Surface micromachining allows flexible design, but offers poor mechanical and optical properties, due to the use of deposited layers that are often thin and curved. LIGA provides high sidewall verticality, but is restricted to metals and plastics. DRIE of BSOI is a useful compromise, since it allows arbitrary features in thick layers of high-quality single crystal material. The processes have been used to form fixtures for miniature, hybrid-integrated components, and also fully integrated systems.

The most common bulk components are optical fibres, lenses, filters, lasers, and detectors. Standard silica telecommunications fibre has an outer diameter of 125 μm and a core diameter of 8 μm. Anisotropic etching has been used to form kinematic mounts for fibres [**13**], fibre cable connectors [**14**], and arrangements for connecting fibres to detectors and lasers [**15**, **16**]. These methods have been extended to incorporate planar lightwave circuits in complete opto-hybrid modules [**17**]. Coupling lenses may be in the form of rod lenses [**18**] and spheres [**19**]. Common approaches to collimation include the use of lensed fibres [**20**] and, for shorter propagation distances, thermal diffusion of the core dopant [**21**]. Filters for dense wavelength division multiplexing are often multi-layer stacks [**22**]. Integrated lenses may be formed by a variety of methods, including reflow melting [**23**] (possibly followed by transfer into an underlying layer) or etching of a Fresnel lens pattern [**24**]. Planar micromirrors may be formed using the wafer surface or by vertical etching [**25**]. In-plane

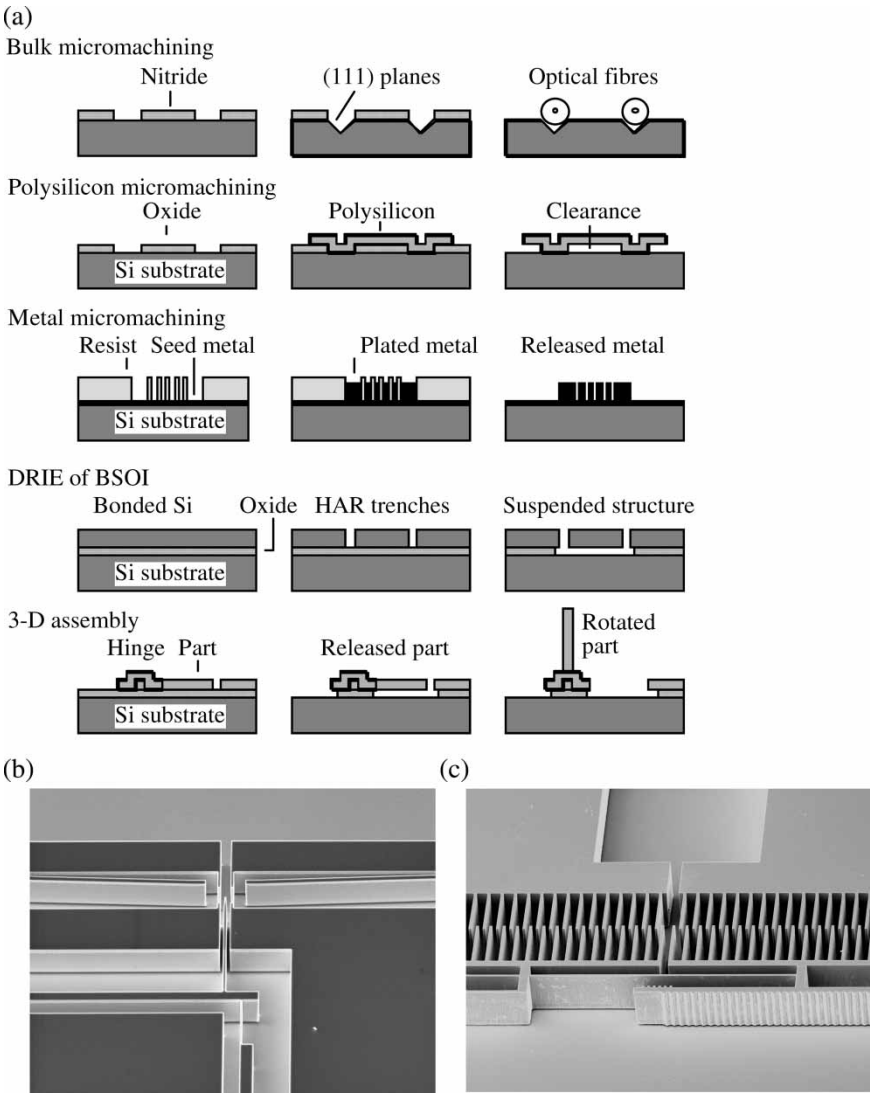

Fig. 1 (a) MEMS fabrication methods; (b) latching VOA; and (c) tuning element for a laser

blazed gratings may be formed by wet chemical etching [**26**], and out-of-plane gratings may be formed by the LIGA process [**27**] or deep silicon etching [**28**].

All fabrication systems allow optical components and elastic supports to be combined with electrostatic or electrothermal actuation. The supports are flexures operating in bending or torsion. One limit to operating speed is therefore set by the mechanical time constant of the resulting mass-spring system. Component size determines mass and operating voltages or drive powers determine stiffness. Resonant frequencies typically lie in the range 100 Hz–100 kHz, which is sufficient for many operations involved in network reconfiguration.

Electrostatic actuators have the advantage of low power; however, high (>200 V) voltages may be required with large electrode gaps. Parallel plate and comb electrodes may be used. The former type is simple to fabricate but complex to control, since it suffers from a pull-in instability [**29**]. The latter is more stable [**30**], but harder to fabricate as a deep structure. Out-of-plane actuators based on vertically staggered comb electrodes have also been developed [**31**]. Although electrothermal actuators consume power continually, they allow large actuation forces from small, light structures. Material bimorphs, which operate by differential thermal expansion in a bilayered cantilever, may be used for both out-of-plane [**32**] and in plane [**33**] motion. Shape bimorphs, which operate by differential expansion between parts of different length or section, also allow in plane motion [**34**]. Buckling mode actuators operate by differential thermal expansion between suspended beams and the substrate and are available quasi-linear [**35**, **36**] and bistable versions [**37**].

Early developments in optical MEMS can be traced to the work of Petersen on scanning mirrors [**38**] and Hornbeck [**39**] on the Texas Instruments Digital Micromirror Display. However, the greatest effort has been expended on devices for telecoms. Advanced packaging (including devices for mounting [**40**], aligning [**41**–**43**] and switching [**44**, **45**] fibres, and mounting and aligning components [**46**]) has been developed. The simplest functional optical MEMS are variable optical attenuators (VOAs), based on the insertion of a shutter between two co-linear fibres [**47**, **48**]. Multiple-blade [**49**, **50**] and latching [**51**] variants have been developed. Figure 1(b) shows a simple shutter insertion device, with spring alignment features for optical fibres. VOAs based on image translation by a translating [**52**] or tilting [**53**] mirror offer improved polarization- and wavelength-dependence of loss.

A modification of the same principle – insertion of a mirror – allows the construction of a small port count switch. Mirrors have been translated [**54**, **55**] and rotated [**56**, **57**] into position, and the devices have been operated in transmission and reflection [**58**]. Larger optical cross-connects (OXC) operate by beam steering [**59**] or using arrays of two-axis tilt mirrors [**60**, **61**]. Optical performance has been improved by replacing polysilicon mirrors with single crystal surfaces [**62**], and electromechanical performance has been improved by replacing parallel plate with terraced [**63**] and vertical comb electrodes [**64**]. An extremely high performance cross-connect has recently been demonstrated by Fujitsu [**65**].

In the signal-processing domain, switch arrays have been combined with dispersive filters to form ADD-DROP multiplexers [**66**] and spectral equalizers [**67**], or with delay lines to form true-time delays [**68**]. A variety of Fabry–Perot filters have been demonstrated [**69**, **70**], and tunable devices have been used for attenuation [**71**] and modulation [**72**] in addition to filtering. Photonic bandgap devices with greatly increased free-spectral range have also been developed [**73**]. Fabry–Perot filters have been combined with vertical cavity surface emitting lasers (VCSEL) to form tunable sources [**74**, **75**]. External cavity lasers have been constructed from semiconductor optical amplifiers (SOAs) using movable mirrors [**76**] and gratings [**77**, **78**]. Figure 1(c) shows a tuning element based on a deep-etched silicon grating mounted on a flexure suspension and driven by a pair of electrostatic comb drives. The most successful device – the Iolon Apollo^{TM} laser – used a hybrid-integrated mirror mounted on a deep etched electrostatically driven rotation stage with a fixed grating in a Littman configuration [**79**].

3 GAUSSIAN BEAMS

In this section it is shown how Gaussian beams propagate in gradient-index (GRIN) media such as optical fibres, and then describe how their behaviour is modified in free space.

Suitable models for weakly guiding optical systems may be constructed using scalar theory, based on the time-independent Helmholtz equation, written in Cartesian co-ordinates as

$$\frac{\partial^2 E}{\partial x^2} + \frac{\partial^2 E}{\partial y^2} + \frac{\partial^2 E}{\partial z^2} + n^2 k_0^2 E = 0 \tag{1}$$

Here $E(x, y, z)$ is the time independent electric field, n is the refractive index, and $k_0 = 2\pi/\lambda$ is the free space propagation constant, where λ is the wavelength. In free space, equation (1) has the solution $E = E_0 \exp(-jk_0 z)$ for z-propagating plane waves. However, because of the small size of microoptical systems, a single plane wave solution is inappropriate.

Graded-index fibres generally have a parabolic radial variation in dielectric constant, as shown in

Fig. 2(a). Near its axis, the refractive index n of a z-oriented fibre varies as $n^2 = n_0^2\{1 - (r/r_0)^2\}$. Here n_0 and r_0 are constants and $r^2 = x^2 + y^2$. For radially symmetric guided modes, it may be assumed that $E(r, z) = E_T(r)\exp(-j\beta z)$, where E_T is the transverse field and β is the propagation constant. Equation (1) can then be reduced to the scalar waveguide equation

$$\frac{d^2E_T}{dr^2} + \left(\frac{1}{r}\right)\frac{dE_T}{dr} + \left\{n_0^2k_0^2\left[1 - \left(\frac{r}{r_0}\right)^2\right] - \beta^2\right\}E_T = 0 \tag{2}$$

It is simple to show that the Gaussian transverse field $E_T(r) = E_0\exp(-r^2/a^2)$ is a solution, and that the mode radius a and propagation constant β are given by $a = \sqrt{(2r_0/n_0k_0)}$ and $\beta^2 = n_0^2k_0^2 - 4/a^2$ [**6**]. As a result, all graded index media support Gaussian modes. Single-mode fibre often has a parabolic index variation because it gives low signal dispersion, and a small mode, with $a \approx 4\,\mu m$ at near-infrared ($1.5\,\mu m$) wavelength.

Using rectangular coordinates, it can be shown that higher-order solutions are Hermite–Gaussian modes, with transverse fields $E_{\mu\nu}(x, y) = H_\mu(\sqrt{2}x/a)H_\nu(\sqrt{2}y/a)$ $\exp[-(x^2 + y^2)/a^2]$. Here μ and ν are mode numbers, and $H_\mu(\zeta)$ is a Hermite polynomial of order μ. From standard texts, $H_0(\zeta) = 1$, $H_1(\zeta) = 2\zeta$, $H_2(\zeta) = 4\zeta^2 - 2$, $H_3(\zeta) = 8\zeta^3 - 2\zeta$, and so on. Figure 2(b) shows the first few functions $H_\mu(\sqrt{2}x/a)\exp(-x^2/a^2)$. The Gaussian solution above is the lowest-order mode, with $\mu = \nu = 0$. The complete mode field patterns are multi-lobed, with the number of lobes increasing with μ and ν; the insets show the variations of E_{10} and E_{21}.

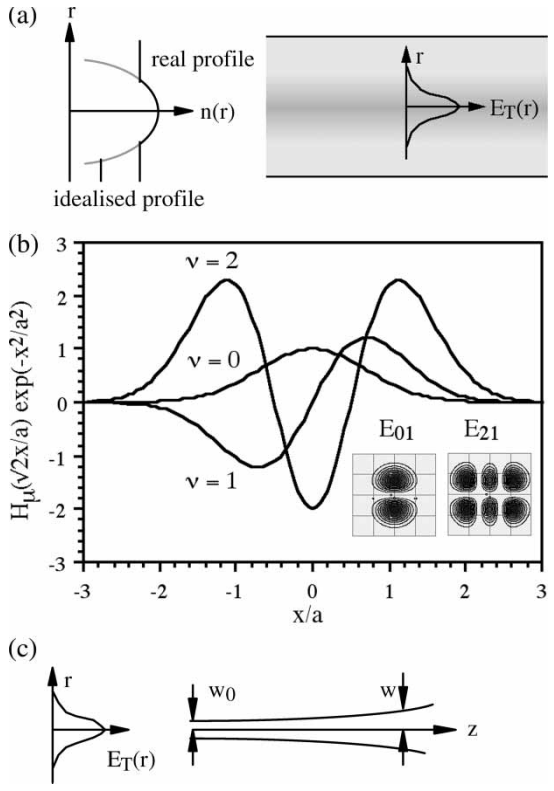

Fig. 2 (a) Index profile and Gaussian mode of a parabolic index fibre; (b) three functions $H\nu(\sqrt{2}x/a)\exp(-x^2/a^2)$; and (c) transverse field and expansion of a Gaussian beam

For weakly guiding systems, the corresponding propagation constants $\beta_{\mu\nu}$ are given by $\beta_{\mu\nu} \approx n_0k_0 - 2(\mu + \nu + 1)/r_0$ [**6**]. The linear dependence of $\beta_{\mu\nu}$ on μ and ν allows imaging functions to be carried out using graded-index media, as show later.

Modal solutions have the property of orthogonality, so that the integral over all space of the product of one mode and the complex conjugate of another is zero

$$\int\int_A E_{\mu\nu}E^*_{\mu'\nu'}\,dx\,dy = 0 \quad \text{for } \mu \neq \mu' \text{ and } \nu \neq \nu' \tag{3}$$

This integral is often written as $\langle E_{\mu\nu}, E_{\mu'\nu'}\rangle$. Orthogonality allows an arbitrary transverse field $E_T(x, y)$ to be expanded as a sum of modes, e.g. as $E_T = \Sigma_\mu\,\Sigma_\nu\,a_{\mu\nu}E_{\mu\nu}(x, y)$. Multiplying both sides by $E_{\mu'\nu'}$ and integrating, the expansion coefficients can be found as $a_{\mu\nu} = \langle E_T, E_{\mu\nu}\rangle/\langle E_{\mu\nu}, E_{\mu\nu}\rangle$. This expression is simple to evaluate if fields are normalized, so that the denominator is unity. It is simple to show that the power carried by each mode is proportional to $|a_{\mu\nu}|^2$.

Gaussian beams can also express the effects of diffraction in free space. Since they are effectively bounded plane waves, solutions to the wave equation may be assumed in the form of modified plane waves. For cylindrically symmetric z-propagating fields, therefore, it is assumed that $E(r, z) = E_0A(r, z)\exp(-jk_0z)$, where A is a slowly varying function. Substituting into equation (1), and neglecting $\partial^2A/\partial z^2$

$$\frac{\partial^2A}{\partial r^2} + \left(\frac{1}{r}\right)\frac{\partial A}{\partial r} - 2jk_0\frac{\partial A}{\partial z} = 0 \tag{4}$$

It is simple to show that $A = E_0\exp[-j(p + k_0r^2/2q)]$ is a solution [**6**]. Here p and q are only functions of z, and q is the complex beam parameter. Substituting into the above

$$2k_0\left(p' + \frac{j}{q}\right) + \left(\frac{k_0^2r^2}{q^2}\right)(1 - q') = 0 \tag{5}$$

Here, the prime indicates differentiation with respect to z. The terms in curly brackets must both vanish, so that $q' = 1$ and $p' = -j/q$. However, the term $\exp(-jp)$ in the solution contains z alone, whereas $E_T(r, z) = E_0\exp(-jk_0r^2/2q)$ also depends on r.

Ignoring the first term, and assuming that $q = z + jz_0$, where $z_0 = k_0 w_0^2/2$

$$E_T(r, z) = E_0 \exp\left(\frac{-r^2}{w^2}\right) \exp\left(\frac{-jk_0 r^2}{2R}\right) \quad (6)$$

Here, the new parameters w and R have been introduced, given by $w^2 = w_0^2 (z_0^2 + z^2)/z_0^2$ and $R = (z_0^2 + z^2)/z$. Equation (6) describes a Gaussian beam varying as $E_T(r, z) = E_0 \exp(-r^2/w_0^2)$ on $z = 0$. Away from this plane, the more general term $\exp(-r^2/w^2)$ describes the radial amplitude variation, whereas $\exp(-jk_0 r^2/2R)$ is a radial variation in phase that implies the phase-front is curved. The parameter w is the local beam radius, whereas R is the radius of curvature of the phase-front. Both vary with z, on a scale characterized by the distance z_0. The term $\exp(-jp)$ is needed for power conservation. It can be written as $jz_0/(z + jz_0)$ or q_0/q, where q_0 is the value of q at the waist. For small z, this term is roughly constant, whereas for large z it decays as $1/z$. Near the waist, the beam is narrow and the phase-front is flat ($z \ll z_0$). Far from the waist ($z \gg z_0$), it diverges as a spherical wave. Figure 2(c) shows the variation of w with distance. As one might expect, free-space equivalents of Hermite–Gaussian modes also exist, and can be used to model arbitrary fields. Their properties have been used to explain the behaviour of cavity resonators and lens waveguides [**5**, **6**].

Because the field at the waist of a free-space Gaussian is similar to the mode supported by a graded-index fibre, the former is an extension of the latter, and the wave emerging from a cleaved fibre will expand as predicted by equation (6). For the small modes of single-mode fibres, the expansion is rapid. For $a = 4\ \mu m$ and $\lambda = 1.5\ \mu m$, for example, $z_0 = 33\ \mu m$. Consequently, imaging components are used to transform the beam, a process, which alters the value of w_0 and hence controls any subsequent expansion.

4 BEAM CONTROL

In this section, it is shown how one free-space Gaussian beam can be converted into another with a lens, based on GRIN and refractive optics.

As previously described, a forward-travelling field $E(x, y, 0)$ specified on the plane $z = 0$ of a GRIN medium may be expanded in Hermite–Gaussian modes. After a distance z, this field will be modified to $E'(x, y, z) = \Sigma_\mu \Sigma_\nu a_{\mu\nu} E_{\mu\nu}(x, y) \exp(-j\beta_{\mu\nu} z)$. Inserting the propagation constants, $E'(x, y, z) = \exp(-j\psi) \Sigma_\mu \Sigma_\nu a_{\mu\nu} E_{\mu\nu}(x, y) \exp[j(\mu + \nu)z/r_0]$, is obtained where $\psi = (k_0 n_0 - 1/2r_0)z$ is a constant phase shift. If $z = 2\pi r_0$, the additional phase shift seen by each mode is a whole number of multiples of 2π. At this point, E' differs from E only by the complex exponential $\exp(-j\psi)$. Propagation through a distance $P = 2\pi r_0$ (the pitch length), therefore, leaves the field effectively unchanged. This process may be viewed as creating a real, upright image of the input, as a lens does. GRIN lenses are short lengths of graded-index media with polished ends, formed by ion exchange with much larger values of r_0 than fibres. Propagation through half a pitch inverts all modes with odd $\mu + \nu$, and therefore, forms an inverted real image I of an object O as shown in Fig. 3(a). Propagation through a quarter-pitch forms an image at infinity of an axial point object. GRIN lenses used in fibre coupling have standard lengths of just less than $P/2$ and $P/4$ [**18**].

Although GRIN lenses provide elegant packaging solutions, simpler alternatives are often used. The thin lens has spherical surfaces of radii R_1 and R_2. In a material of refractive index n, the focal length f is given by the lens-maker's formula $1/f = (n - 1)(1/R_1 + 1/R_2)$. For a plano-convex lens (which has,

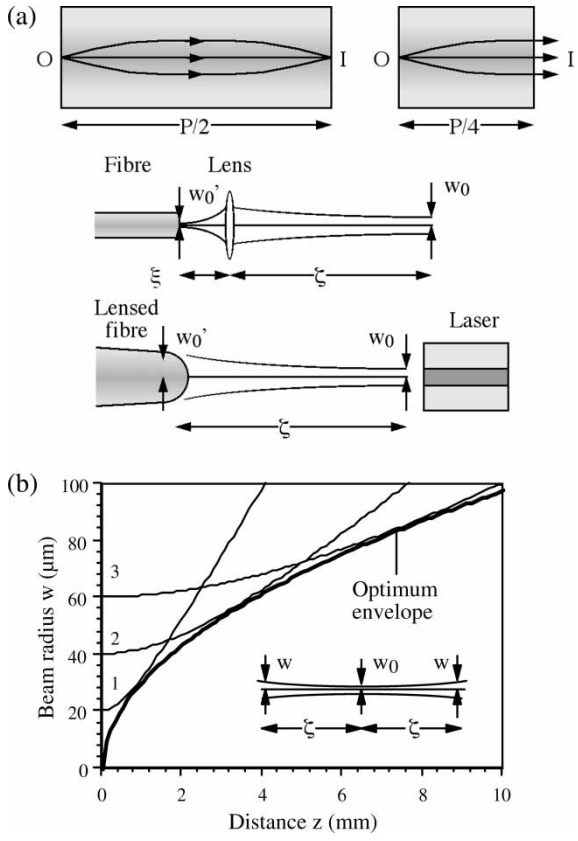

Fig. 3 (a) Imaging behaviour of GRIN-rod lenses, thin lenses, and lensed fibre and (b) variation of Gaussian beam radius with distance for $\lambda = 1.5\ \mu m$ and three values of w_0 (1–20 μm, 2–40 μm, and 3–60 μm)

for example, R_2 infinite), $f = R_1/(n-1)$. For a spherical ball lens ($R_1 = R_2$), $f = R_1/(2(n-1))$. Since a ball lens is physically thick, the lens-maker's formula is not strictly valid, but this estimate gives a reasonable start.

If a lens of focal length f is placed a distance ξ away from a Gaussian waist of radius w_0' as shown in Fig. 3(a), the beam will have diverged to a radius w' and its phase-front will have radius R' at the lens. To create an expanded beam with a waist w_0 a distance ζ away from the lens, it is assumed that the lens corrects the phase-front according to the imaging equation $1/R + 1/R' = 1/f$. In the process, $w' = w$. After some manipulation, it can be shown that the focal length is the solution of the two alternative quadratic equations [**6**]

$$(M^2-1)f^2 + 2\zeta f - (M^2 f_0^2 + \zeta^2) = 0 \quad \text{or}$$
$$\left(\frac{1}{M^2} - 1\right)f^2 + 2\xi f - \left(\frac{f_0^2}{M^2} + \xi^2\right) = 0 \tag{7}$$

Here, the magnification $M = w_0/w_0'$ and the normalized distance $f_0 = (\pi/\lambda)w_0 w_0'$ must be introduced. It can also be shown that the object and image distances are related by

$$\zeta = f \pm M\sqrt{(f^2 - f_0^2)} \quad \text{and}$$
$$\xi = f \pm \frac{1}{M}\sqrt{(f^2 - f_0^2)} \tag{8}$$

The formulae above provide a first line of attack on micro-optical system design problems.

Often, a fibre must be coupled to a semiconductor laser. Lasers have very small mode sizes, because of their large index steps. Their modes can be described approximately by a circular mode whose radius is the geometric mean of orthogonal half-widths. A lens that can demagnify the fibre mode is therefore required; this can be constructed by melting the end of a tapered fibre, as shown in Fig. 3(a). In this case, the object distance ξ is zero. From the above, $f = f_0/(1 - M^2)^{1/2}$. If M is small, $f \approx f_0 \approx (\pi/\lambda)(w_0 w_0')$. The required lens radius is then $R_1 = (n-1)f$. For example, assuming that $n = 1.46$ (for silica), $w_0' = 4\ \mu\text{m}$, $w_0 = 1\ \mu\text{m}$, and $\lambda = 1.5\ \mu\text{m}$, $f = 8.38\ \mu\text{m}$ and $R_1 = 3.85\ \mu\text{m}$ are obtained. The fibre end must therefore be tapered down to around 8 μm diameter and then melted to a hemisphere. The distance between lens and laser is $\eta \approx f$, implying stringent axial alignment tolerances.

The propagation of a Gaussian beam can be modelled using the complex beam parameter $q = z + jz_0$. It is simple to show that q is related to w and R by $1/w^2 = -(k_0/2)\,\text{Im}(1/q)$ and $1/R = \text{Re}(1/q)$. The effect of propagation through a distance z, or through a lens of focal length f, is to modify q. The new value q' is given by the *ABCD* rule $q' = (Aq + B)/(Cq + D)$ [**5**]. It is simple to show from earlier results that the coefficients A, B, C, and D are

	A	B	C	D
Propagation through a distance z	1	z	0	1
Propagation through a lens	1	0	$-1/f$	1

(9)

The *ABCD* method may simulate propagation of perfect Gaussian beams through arbitrary optical systems, and also Hermite–Gaussian beams in a more general field. If the system contains mirrors, it is simply unfolded. If any mirror is curved, it can be replaced with an equivalent spherical lens. For a concave mirror of radius r, the focal length is $f = r/2$.

More complicated wave-fronts cannot be propagated as described above, and diffraction theory must be used. In this case, the diffraction of an optical field E specified on the (x, y) plane to a field E' on the (x', y') plane a distance z away is described by the integral

$$E'(x', y') = \int\int_A \left\{\frac{f(\theta)}{j\lambda_0\rho}\right\} E(x, y)\exp(-jk_0\rho)\,\mathrm{d}x\,\mathrm{d}y \tag{10}$$

Here $\rho = \sqrt{[(x'-x)^2 + (y'-y)^2 + z^2]}$ is the distance between the points (x, y) and (x', y'), and $f(\theta)$ is a slowly varying angular function designed to exclude backward travelling waves. For normal incidence on the object plane, $f(\theta) = [1 + \cos(\theta)]/2$, where θ is the angle between the z-axis and the vector $\mathbf{r} = (x' - x)\mathbf{i} + (y' - y)\mathbf{j} + z\mathbf{k}$.

5 OPTIMUM BEAM DESIGN

Compact systems require minimized beam sizes. The optimum arrangement to travel a distance 2ζ is then as shown in Fig. 3(b). Here, the beam converges to a symmetrically placed waist and then diverges. Figure 3(b) also shows the variation of w with z obtained for different initial beam widths w_0, assuming that $\lambda = 1.5\ \mu\text{m}$. In each case, w is roughly constant for small z, and then increases rapidly. Curve 1 ($w_0 = 20\ \mu\text{m}$) provides a smaller beam for short distances than curve 2 (for $w_0 = 40\ \mu\text{m}$). However, the reverse is true for large distance, suggesting that there is an optimum w_0 to travel a given distance ζ. This optimum value is [**7**]

$$w_{0\text{opt}} = \sqrt{\left(\frac{2\zeta}{k_0}\right)} = \sqrt{\left(\frac{\lambda\zeta}{\pi}\right)} \tag{11}$$

The bold locus in Fig. 3(b) shows this envelope, which provides a lower bound to the size of all Gaussian beams. Consequently there is indeed an optimum design; the optimum waist radius scales as the square root of the propagation distance, and ζ is the characteristic distance z_0. It can also be shown that the final radius is $w_{\text{opt}} = w_{0\text{opt}}\sqrt{2}$.

Single-mode fibres may be joined directly, or be separated by a gap to allow insertion of a component such as a shutter. Alternatively, the fibre mode may be expanded by diffusion of the core dopant to allow a larger separation without diffraction losses [**21**]. To form a demountable connection, a quarter pitch GRIN-lens can be used to collimate the fibre output. Two collimated fibres yield a connector with a large tolerance of transverse alignment errors [**19**]. Using components such as multi-layer filters or gratings, larger waists are required. The beam is therefore allowed to diverge from the input fibre and an optimum Gaussian is created using a lens, as shown in Fig. 4(a). A second lens is then used to couple the beam back into an output fibre. When simpler components such as mirrors are used, or a very compact system is required, lensed fibres can create a mid-point waist smaller than the fibre mode.

An optimized layout may be designed very simply. First, equation (11) is used to find the half-length ζ of the expanded beam from the desired value of w_0. Equation (7) is then used to find the focal length f of the lens from the values of ζ and the mode size w_0' of the fibre. Equation (8) is then used to find the object position ξ. Figure 4(b) shows a design example. Here a 16-μm waist radius is generated from 4-μm mode radius at $\lambda = 1.5$ μm, over a path length $2\zeta =$ 1 mm, and the *ABCD* method has been used to find the variations of w and $1/R$.

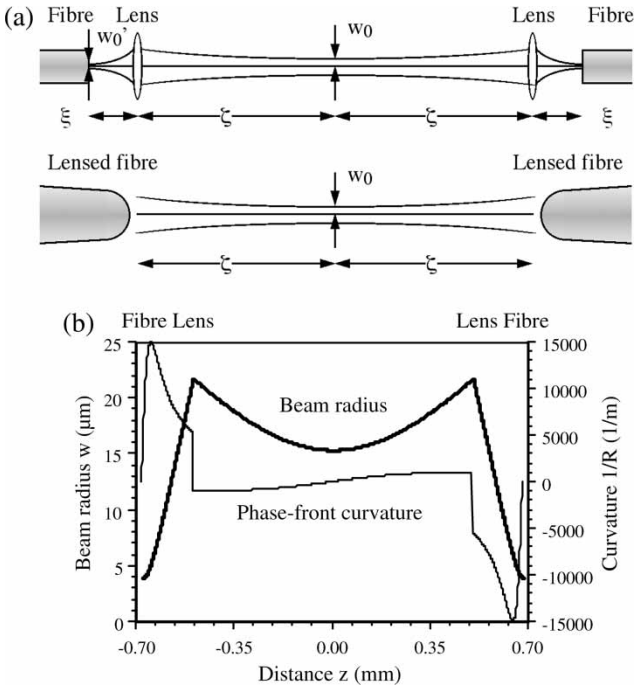

Fig. 4 (a) Free-space fibre-to-fibre links and (b) variation of beam radius and curvature with distance for fibre-lens-lens-fibre link with $2\zeta = 1$ mm, $a = 4$ μm, and $\lambda = 1.5$ μm

6 COUPLING AND ALIGNMENT

Generally, the problem is to design a system with high end-to-end throughput (although dispersion and polarization sensitivity may also be important). In this case, the coupling efficiency into the desired output device (often, a fibre) must be found. From modal orthogonality, it can be shown that the coupling efficiency of a field E_{T1} into a guide supporting a transverse field E_{T2} may be found as

$$\eta = \frac{|\langle E_{\text{T1}}, E_{\text{T2}}\rangle|^2}{\{\langle E_{\text{T1}}, E_{\text{T1}}\rangle \langle E_{\text{T2}}, E_{\text{T2}}\rangle\}} \tag{12}$$

This expression can be used to find the coupling efficiency in imperfect systems, and hence establish tolerances. Examples include the misaligned fibre joints shown in Fig. 5(a).

For example, if the input is a Gaussian, misaligned by δ_y in the transverse direction from a fibre supporting a similar mode, then $E_{\text{T1}}(x, y) = E_0 \exp\{-[x^2 + (y - \delta_y)^2]/a^2\}$ and $E_{\text{T2}}(x, y) = E_0 \exp[-(x^2 + y^2)/a^2]$. In this case, the efficiency is $\eta(\delta_y) = \exp(-\delta_y^2/a^2)$. For small errors, $\eta(\delta_y) \approx 1 - (\delta_y/a)^2$. The coupling loss, defined in decibels as $-10\log_{10}(\eta) = 4.343\,\delta_y^2/a^2$, therefore, rises parabolically with the transverse error δ_x. Here, what is important is the size of δ_y compared with the mode radius. For losses below 1 dB (the maximum allowable in a low loss system), $\delta_y/a < 0.5$ is required. For $a = 4$ μm, then $|\delta_y| < 2$ μm is required. This tolerance is clearly relaxed by increasing the mode radius.

Similarly, if the input is separated axially from the output by a distance δ_z, an overlap may be taken between the fields $E_{\text{T1}} = E_0 \exp(-r^2/w^2)$ $\exp(-jk_0r^2/2R)$ and $E_{\text{T2}} = E_0 \exp(-r^2/a^2)$ to get

$$\eta = \frac{4w^2a^2}{[(w^2 + a^2)^2 + (k_0w^2a^2/2R)^2]} \tag{13}$$

Assuming that $w_0 = a$ and $z = \delta_z$, $\eta(\delta_z) = 1/[1 + (\delta_z/2z_0)^2]$ is obtained. Since z_0 is relatively large, axial alignment tolerances are larger than transverse ones. Figure 5(a) shows the variation of η with δ_z/z_0.

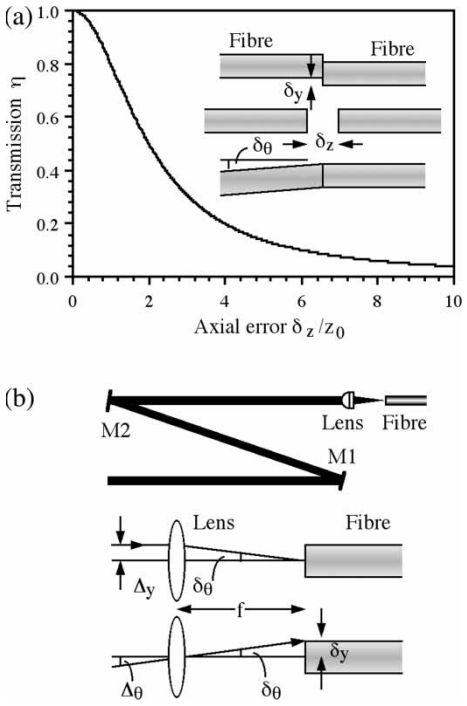

Fig. 5 (a) Variation of fibre-fibre coupling loss with axial misalignment and (b) free-space input coupling with misalignment

For losses below 1 dB, $\delta_z/z_0 < 1$ is required. The tolerance is relaxed using index-matching fluid, because z_0 increases to $k_0 n w_0^2/2$ in a medium of index n.

Similarly, if the input is on-axis, but skewed by a small angle δ_θ, it can be written as (for example) $E_{T1}(x, y) = E_0 \exp[-(x^2+y^2)/a^2]\exp(-jkx\delta_\theta)$, with $E_{T2}(x, y)$ as before. Then $\eta(\delta_\theta) = \exp(-\pi^2 a^2 \delta_\theta^2/\lambda^2)$ is obtained. The loss rises parabolically with the skew angle, and for losses below 0.1 dB, $\pi a\delta_\theta/\lambda < 0.1$ is required. Assuming that $a = 4\ \mu$m and $\lambda = 1.5\ \mu$m, $|\delta_\theta| < 0.018$ rad, or 1° is then obtained. This time, what is important is the phase shift $\phi = 4\pi a\delta_\theta/\lambda$ across the beam. In contrast to the previous example, increasing the mode radius increases loss, because it increases the phase shift. There may be additional transverse and angular alignment errors δ_x and δ_ψ. Because the effects are separable, the overall efficiency may be estimated from the product $\eta = \eta(\delta_x)\,\eta(\delta_y)\,\eta(\delta_z)\,\eta(\delta_\theta)\,\eta(\delta_\psi)$.

Similar analysis may be used to find the efficiency obtained when a free-space beam is coupled back into a guided mode using a lens spaced approximately f away. The beam may (for example) strike the lens on-axis, but with a lateral offset Δ_y as shown in Fig. 5(b). At the fibre, the result will be an angular error $\delta_\theta \approx -\Delta_y/f$. Alternatively, it may strike the lens at an angle Δ_θ, resulting in both an angular error $\delta_\theta = \Delta_\theta$ and a transverse error $\delta_y = f\Delta_\theta$. The errors may then be combined, and the product expression used to find the efficiency. Clearly, the need for accurate alignment increases as the system size rises. At first sight, it would seem that a pair of mirrors $M1$ and $M2$ arranged as a periscope, and capable of tilting about two orthogonal axes, should be able to align any input beam with a fibre. Unfortunately, it is difficult to identify the different contributions to loss simply by measuring throughput. Alignment is therefore optimized by successive adjustment of each axis in turn, using dither to accelerate the process, and recording the final positions.

7 OPTICAL SURFACE CURVATURE

Arrangements of the type in Fig. 5(b) are often used in switches and the mirrors are then fabricated as MEMS parts. Because of coating stress, their surfaces may be curved, and it important to estimate the maximum curvature that may be tolerated.

The simplest way to find the effect of imperfect surfaces is to unfold the system, replacing each curved surface with an equivalent lens. The *ABCD* method may then be used to propagate the beam between input and output. Knowing the values of w and R on exit, the coupling efficiency may be found. For example, Fig. 6(a) shows such an arrangement, with a curved mirror located at a distance z from the waist. Fig. 6(b) shows the variation of beam radius with position, for $2\zeta = 1.0$ mm, $z/z_0 = 0.33$, $a = 4\ \mu$m, $\lambda = 1.5\ \mu$m, and different values of the focal length f of the equivalent lens. For large f, there is little deviation from the optimized arrangement shown in Fig. 4(b). As f reduces, the beam is focused more and more, so that the final mode no longer has the correct radius to couple into the output fibre.

An analytic estimate of the effect of a single curved surface may be found by the realization that only a single Gaussian will couple optimally into the output fibre; all others are coupled suboptimally. In the absence of the surface curvature, it might be assumed that the system provides this beam. Although the system may contain several optical elements, each one then merely transforms the beam parameters to provide the optimum output. Hence, the coupling efficiency may be evaluated at the curved surface itself in terms of an overlap between the local beam with and without the surface curvature; there is no need to propagate to the output. To implement this plan, a method is needed to find the overlap between two beams, the second of which is transformed by a lens simulating the curved surface at an arbitrary position z. If the integrals in equation (3) are performed using the full solution $A(r, z)$ and the complex beam parameter q, the

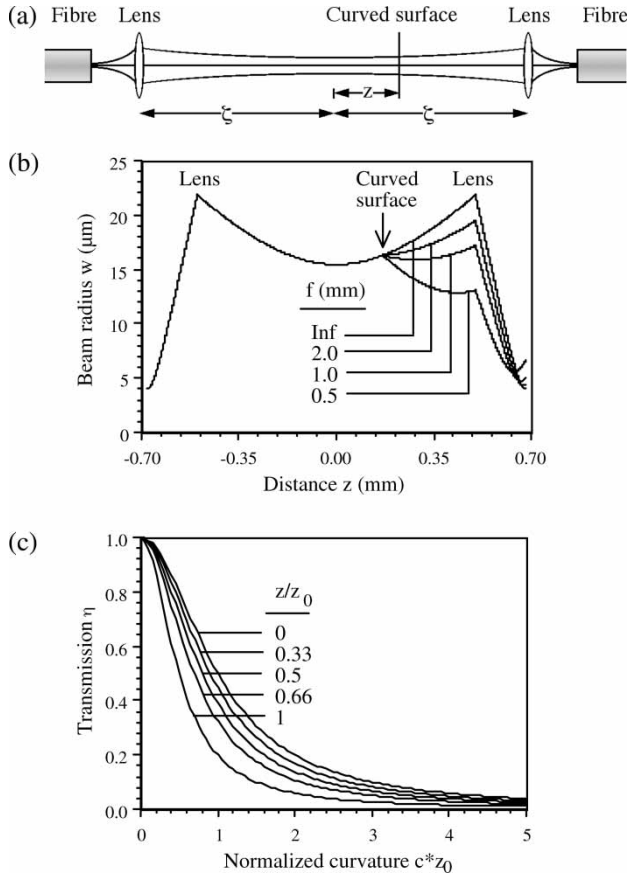

Fig. 6 (a) Fibre-to-fibre link with curved surface en route; (b) example variations of beam radius with distance; and (c) variations of transmission with surface curvature

following is obtained for two fields A_1 and A_2

$$\langle A_1, A_2\rangle = j\left(\frac{2\pi E_0^2}{k_0}\right) q_{01} q_{02}^* (q_1 - q_2^*) \tag{14}$$

Here q_{01} and q_{02} are the waist values of q_1 and q_2. Other terms $\langle A_1, A_1\rangle$ and $\langle A_2, A_2\rangle$ may be found in a similar way. To model the effect of a curved surface, equation (16) is evaluated with $q_2 = q_1/(1 - q_1/f)$ as required by the *ABCD* method and the result is used in equation (12) to find the efficiency. In terms of the element curvature $c = 1/r$, the following is obtained

$$\eta = \frac{1}{\{1 + (cz_0)^2[1 + (z/z_0)^2]^2\}} \tag{15}$$

Equation (15) gives the transfer efficiency for any system with a single, arbitrarily located curved surface, in terms only of simple local parameters. Since it is quadratic in f and z, converging and diverging elements have the same effect, as do surfaces on either side of the waist. Figure 6(c) shows the variation of η with cz_0, for different values of z/z_0. The efficiency falls rapidly with cz_0. The allowable curvature decreases inversely with the system size, and long propagation paths require very flat mirrors, ideally formed in single crystal Si [**62**].

8 VARIABLE OPTICAL ATTENUATORS

Devices based on movable optical components are now considered, which begins with VOA, which may be constructed using beam translation or shutter insertion.

Figure 7(a) shows a beam translation VOA, which operates by moving a small mirror in the optical path between two fibres with perpendicular axes [**47**]. If the mirror translates laterally by δ_y, the beam will deviate from alignment at the output by the same amount, so the transfer efficiency will be $\eta(\delta_y) \approx 1 - (\delta_y/a)^2$. In this example, the path length is one fibre diameter, so diffraction losses are to be expected. However, the path may be shortened, by bringing the fibre ends closer together using tapered lensed fibres. The angle between the fibre axes may also be reduced to lessen the polarization

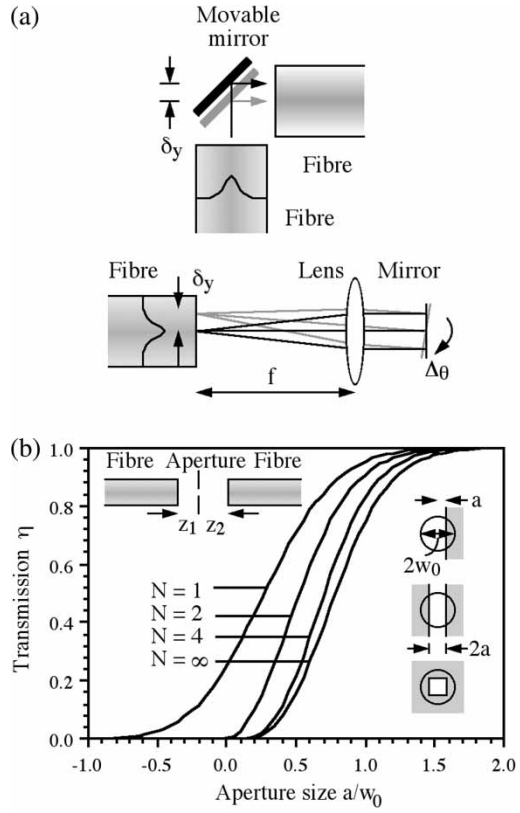

Fig. 7 (a) Beam translation VOAs based on mirror insertion and mirror tilt; and (b) variation of transmission with normalized aperture a/w_0 for shutter insertion VOAs

dependence of mirror reflectivity. Figure 7(a) also shows a reflective VOA that operates on a similar principle, but using the combination of a lens and a tilting mirror to achieve beam translation. If the tilt mirror is close to the lens and the focal length is relatively long, the lateral translation is $\delta_y \approx 2f\Delta_\theta$.

Shutter-based VOAs operate by using one or more movable blades to create a variable aperture between two axially aligned fibres, as shown in Fig. 7(b). Single-blade, double-blade, and square iris VOAs have all been demonstrated [**49**, **50**]. Reduced polarization dependence is expected as the shape of the iris tends to a circle. The effect of the aperture may be described by a function A, whose transmission is unity inside the aperture and zero outside it. Ignoring diffraction, analytic expressions may be obtained for the coupling efficiency of an apertured Gaussian into the output fibre. Assuming the apertured field is $E_{T1} = AE_0 \exp[-(x^2 + y^2)/a^2]$, and that $E_{T2}(x, y) = E_0 \exp[-(x^2 + y^2)/a^2]$, the transfer efficiency η_N of different N-blade polygonal apertures are

$$\eta_1 = \frac{[1 + \mathrm{erf}(\sqrt{2a/w_0})]^2}{4}$$

$$\eta_2 = \mathrm{erf}^2\left(\frac{\sqrt{2a}}{w_0}\right)$$

$$\eta_4 = \mathrm{erf}^4\left(\frac{\sqrt{2a}}{w_0}\right)$$

$$\eta_\infty = \left[1 - \exp\left(\frac{-2a^2}{w_0^2}\right)\right]^2 \tag{16}$$

Here erf(x) is the error function [**80**]. Figure 7(b) shows the variation of transmission in each case. The transmission rises smoothly from zero to unity as the aperture opens, and the travel required ranges from two to three times the beam radius. More generally, when the distances z_1 and z_2 are such that diffraction cannot be ignored, equation (10) may be used to propagate the beam and numerical integration of equation (12) to find the efficiency [**50**].

9 OXC SWITCHES

More complex systems are constructed using multiple movable components. The first example is the OXC, which can operate using mirror insertion and mirror rotation. Scaling laws, determined by diffraction, control switch sizes [**7**].

Figure 8(a) shows a reflective 2×2 mirror-insertion switch [**58**]. Here a pair of quarter-pitch GRIN lenses forms an inverted real image of one

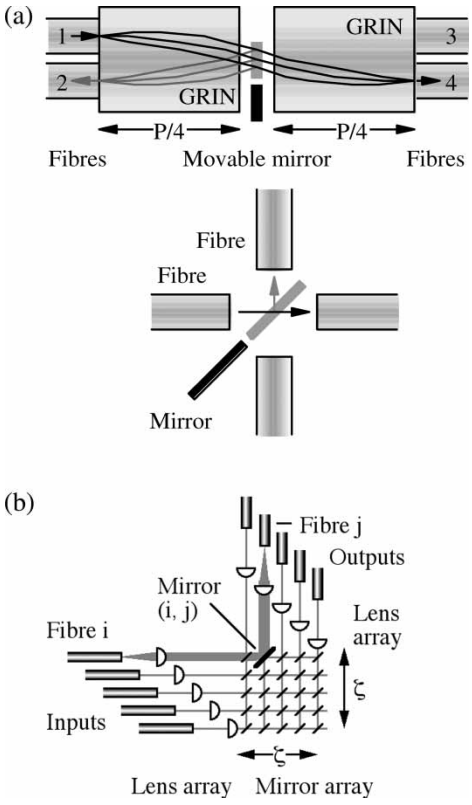

Fig. 8 (a) 2×2 mirror insertion switches and (b) mirror insertion OXC

one pair of fibres on another, so that (for example) ports 1 and 4 are connected. Insertion of a small mirror can cause the image to be reflected, so that the connection now switches to ports 1 and 2. Figure 8(a) also shows a transmissive switch, which combines a pair of intersecting free-space fibre-to-fibre links with a movable mirror [**54**]. Without the mirror, axially aligned fibre pairs are connected. When the mirror is inserted, orthogonal fibres are linked. Several approaches including linear translation and rotation have been used to manipulate the movable mirror.

Figure 8(b) shows how this concept may be scaled to an $N \times N$ switch [**55**–**57**]. Because of the increase in path length, lenses must now be used to control the free-space beams and fibres and lenses must be staggered to equalize optical paths. Connection between the ith and jth fibres is achieved by insertion of the (ith, jth) mirror. Using the optimum Gaussian beam equation, it is simple to derive size-scaling laws for this arrangement. To allow a beam to pass through a lens without significant attenuation, the lens diameter must be significantly greater than the beam diameter – say, $2\alpha w_{opt}$, where w_{opt} is the the beam radius at the lens and α is a constant of order 2. To reasonable approximation, the path length ζ must

then be $\zeta = 2\alpha w_{\text{opt}} \times N$. Using equation (11)

$$\zeta = \frac{8N^2\alpha^2\lambda}{\pi} \tag{17}$$

This result implies that the size of an $N \times N$ cross-connect must increase as the square of the number of ports. It is relatively unfavourable, and suggests a low upper limit to size.

More favourable scaling is obtained for the mirror rotation OXC in Fig. 9(a) [**60**–**65**]. Here the input and output fibre arrays are now square $N \times N$ bundles, so the switch will be $M \times M$ where $M = N^2$. The fibre inputs are collimated by a lens array, and the collimated beams strike an $N \times N$ array of small mirrors on gymbal mounts, which may rotate through small angles about two orthogonal axes. The mirrors redirect the beams to a second $N \times N$ mirror array, which in turn pass them via a second lens array to an output fibre bundle. Because the beams pass each other in space, arbitrary fibre pairs can be linked without crosstalk. If the angles subtended by the mirror arrays are small, the length of the assembly is $\approx 2\zeta/3$. Furthermore, if each mirror has a maximum turn angle of θ, from the previous argument concerning beam size $(2\zeta/3) \times 2\theta = 2\alpha w_{\text{opt}} \times N$. Using equation (11)

$$\zeta = \frac{9M\alpha^2\lambda}{2\pi\theta^2} \tag{18}$$

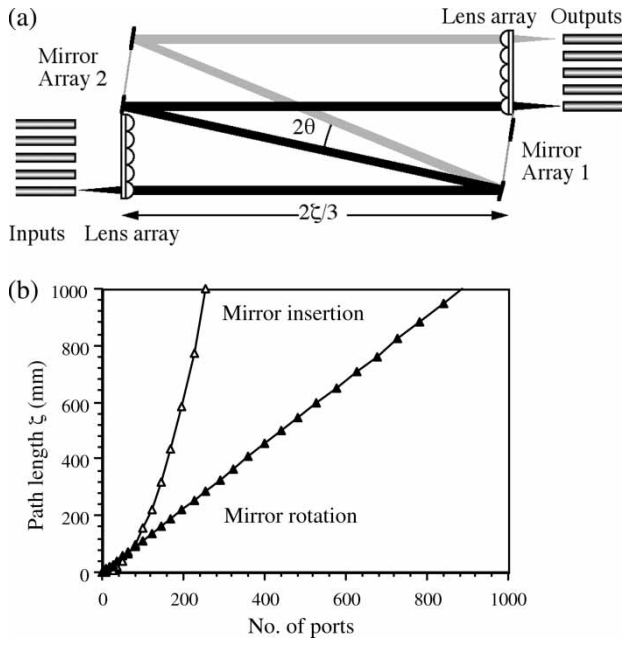

Fig. 9 (a) Large-scale mirror rotation OXC; (b) variation of path length ζ with number of ports for mirror insertion and mirror rotation switches

This time, the switch size scales linearly with the number of ports, so that larger port counts can be obtained with a compact switch. Figure 9(b) shows predictions of the path length ζ needed for both switch types, for $\lambda = 1.5\ \mu\text{m}$, $\alpha = 2$, and $\theta = 5^\circ$. The path length rises with the number of ports, but the advantage of mirror rotation at high port counts is clear. The mirror size scales linearly with ζ, and the tolerable mirror curvature scales inversely.

10 FILTERS AND MULTIPLEXERS

Filtering involves the separation of spectral components. The two common approaches are recursive and dispersive filtering. In the former case, a Fabry–Perot cavity or a multi-layer stack is used to transmit specific components in a band, reflecting the remainder. In the latter, a blazed grating is used to spread the components apart.

It is worth considering the effect on filter performance of bounded beams. Figure 10(a) shows a Fabry–Perot cavity, with two reflecting surfaces L apart, placed at the waist of a Gaussian beam. The overall

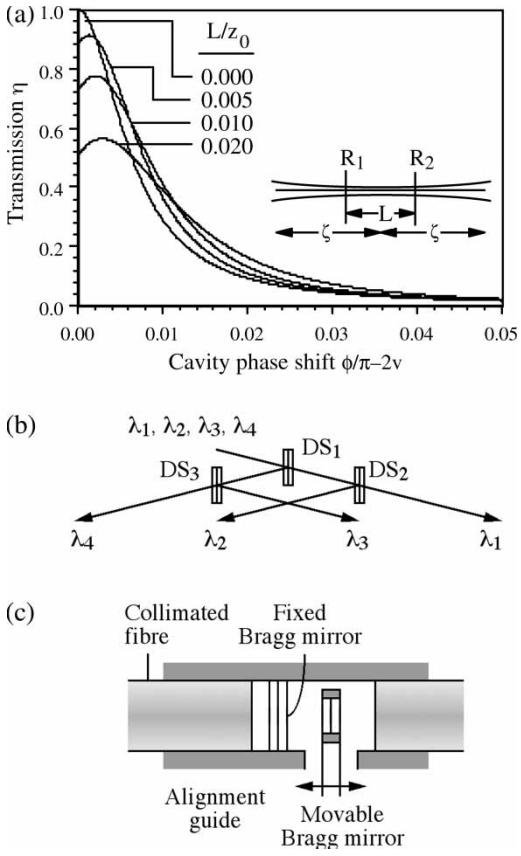

Fig. 10 (a) Variation of Fabry–Perot transmission with cavity phase shift for $R = 0.99$ and different L/z_0; (b) cascaded notch filter; and (c) photonic bandgap filter

transmission is the sum of all possible paths through the device. Defining the transmission and reflection coefficients at the surfaces as T_1 and R_1, and T_2 and R_2, the transmitted field can be obtained at a distance $z > L/2$ as

$$E = E_0 T_1 T_2 \exp(-jk_0 z)\{A(r,z) + \Sigma_{n=1} R_1^n R_2^n \exp(-jn\phi) A(r, z+2nL)\} \quad (19)$$

Here $\phi = 2k_0 L$ is the round trip phase shift. This field is the sum of an infinite set of Gaussian beams, each with different amplitude after travelling a different distance. Generally, this field must be coupled back into a fibre. Unfortunately, it is impossible to define optics that can couple all the components with complete efficiency; only one (say, the first) can be coupled optimally. The overall efficiency may be found using the method in section 7. Carrying out the integrations, and assuming identical mirrors

$$\eta = \left| (1-R^2) \left\{ \frac{1 + \Sigma_{n=1} R^{2n} \exp(-jn\phi)}{(1 - jnL/z_0)} \right\} \right|^2 \quad (20)$$

For $nL \ll z_0$, the standard expression obtained using plane wave analysis is recovered. The effect of the bounded beam is to alter the apparent reflectivity and the cavity resonance condition. For example, Fig. 10(a) shows the variation of η with ϕ, for $R = 0.99$ and different L/z_0. For low L/z_0, the variation is as for an ideal cavity, namely near-unity transmission at $\phi = 2\nu\pi$, where ν is integer, falling rapidly away from this condition. As L/z_0 rises, peak transmission falls, and the bandpass widens and shifts.

It is not surprising that the resonance alters from the classical condition as L/z_0 increases. Away from the waist, where the phase front is almost plane, the full Gaussian solution $A = E_0 \exp[-j(p + k_0 r^2/2q)]$ contains a more complicated z-dependent phase variation than the infinite plane wave $E = E_0 \exp(-jk_0 z)$, which appears in the term $1/(1 - jnL/z_0)$ in equation (20). Because this term is approximately equal to $\exp(jnL/z_0)$, resonance might be expected to occur when $\exp[-jn(\phi - L/z_0)] = 1$, or when $\phi - L/z_0 = 2\nu\pi$. Consequently, the resonance peak shifts slightly as L/z_0 rises. However, the sharpness of the peak degrades because the equality above is only approximate.

The allowed value of L/z_0 depends on the quality of the filter, and wide beams are needed for high finesse. The largest value of z_0 should be used, which again requires optimized Gaussian beams. An alternative is to use mirrors whose curvatures match that of the beam at their respective locations; however, incorrect curvature leads to outputs with rapidly diverging parameters. High performance is generally obtained with flat mirrors on solid substrates or membranes under tension.

Modulators may be constructed from Fabry–Perot cavities with electrostatically deflected membrane mirrors. For example, the mechanical anti-reflection switch, which used a $\lambda/4$ thick dielectric mirror suspended $3\lambda/4$ above the substrate, which was deflected by $\lambda/4$ to modulate the reflection [**71**]. Tunable filters may also be constructed; however, the tuning range is determined from the free spectral range of the cavity. Wider tuning ranges may be achieved using multi-layer reflectors. However, until recently it has been difficult to combine a multi-layer stack with suitable coupling optics and a tuning mechanism at low cost. Figure 10(c) shows a suitable structure [**73**]. The mirrors are vertically etched features, formed by DRIE and crystal plane etching. DRIE of bonded silicon material is used to form alignment features for collimated optical fibres and an electrostatic tuning mechanism.

The multiple resonances in a Fabry–Perot make it difficult to separate channels in a DWDM system. This problem is avoided using dielectric stacks, which allow transmission only over a single band [**22**]. Channel separation may then be carried out using a cascade of filters. Figure 10(b) shows a four-channel filter based on three dielectric stacks. The first element DS_1 is has a broad band-pass, and separates wavelengths λ_1 and λ_2 from λ_3 and λ_4. The elements DS_2 and DS_3 have narrow bandwidths, and separate λ_1 from λ_2, and λ_3 from λ_4, respectively. Assuming the beam is sufficiently wide, the main concern is now to balance losses, by using a tree-structure to equalize the optical paths between input and output.

Dispersive filters may be constructed by combining blazed gratings with suitable optics. Figure 11(a) shows a general structure of period Λ, arranged at an angle θ_0 to a beam of wavelength λ. The direction of the nth diffraction order is given by the grating equation $\sin(\theta_n) = \sin(\theta_0) + n\lambda/\Lambda$. Retroreflection into the -1th order occurs when $\lambda = 2\Lambda \sin(\theta_0)$. If the wavelength is varied, the angle of diffraction varies as $d\theta_{-1}/d\lambda = -1/[\Lambda \cos(\theta_0)]$. The angular dispersion may be converted into a linear dispersion using a lens, so that each wavelength appears spatially separated in the focal plane. Figure 11(b) shows a dispersive demultiplexer, which uses a channel guide pitch converter between the fibre and the lens to reduce the minimum separation between spectral components.

In reverse, a dispersive filter can combine channels, and hence provide a multiplexing function. A combination of multiplexers and switches form a wavelength routing device known as an ADD-DROP MUX, shown in Fig. 11(c). A demultiplexer first separates the INPUT channels. The channels are passed to a set of 2×2 switches, and then to one of two

alternative multiplexers, which recombine them. Depending on the switch states, individual channels are PASSED or DROPPED, and unused switch ports are used to ADD replacements for DROPPED channels. An ADD-DROP MUX can be constructed with a single dispersive multiplexer. Figure 11(c) shows the first MEMS ADD-DROP [**66**], which used an array of tilt mirrors at the focal plane of a lens illuminated by a dispersed beam. High channel density is only obtained with very compact switch elements. Depending on the state of the switches, the channels either retrace their path back to the input, or are routed to a different output. Circulators are used to separate IN and PASS and ADD and DROP signals. A wavelength switch (which has two wavelength-multiplexed inputs) can be constructed similarly, using a second DEMUX before the ADD channels.

11 TUNABLE LASERS

MEMS tunable lasers can be constructed by combining tunable recursive or dispersive filters with a SOA or VCSEL. They offer the potential advantage over monolithic tunable lasers of a simpler tuning algorithm, especially as the laser ages.

Surface emitting lasers may be constructed by combining a VCSEL with a movable dielectric stack, as shown in Fig. 12(a) [**74**]. The device is grown entirely in one step, then etched to create a cantilevered tuning arm. Tuning is achieved by applying a small voltage to the top mirror, which causes the cantilever to deflect vertically so that the laser cavity length is reduced, which in turn alters the emission

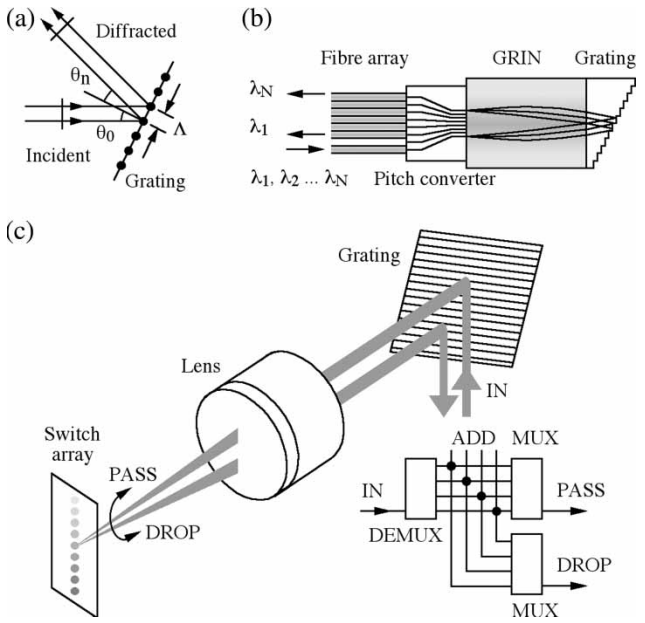

Fig. 11 (a) Grating operation; (b) dispersive filter; and (c) grating-based ADD-DROP multiplexer

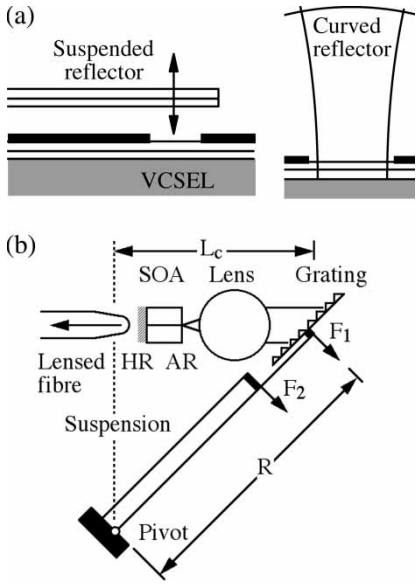

Fig. 12 External cavity lasers based on (a) VCSELS and (b) SOAs

wavelength. A more stable configuration is obtained with a half-symmetric cavity based on a spherically curved reflector [**75**]. The curvature can be achieved by stress; however, it is then difficult to ensure thermal stability.

Alignment tolerances clearly affect laser operation. For example, in an ideal linear model of a laser cavity, the threshold condition is given by $\exp(2gL) = 1/R_1R_2$, where g is the gain constant, L is the length of the gain block, and R_1 and R_2 are the amplitude reflectivities of the two end mirrors. The threshold gain is therefore

$$g = \left(\frac{1}{2L}\right)\log_e\left(\frac{1}{R_1R_2}\right) \tag{21}$$

In any external cavity laser, the primary effect of degrading the alignment of the movable mirror will be to reduce the efficiency η with which the external beam is coupled back into the gain block. As a result, the effective reflectivity of this mirror will reduce to $R_2\sqrt{\eta}$. For example, in the VCSEL of Fig. 12(a), the curvature of the external mirror might be incorrect by an amount Δc. In this case, equation (15) may be used to calculate the coupling efficiency, writing Δc for c. Errors that lead to misalignment, tilt, or axial shift in the reflected beam can be treated using the methods of section 6. The most obvious consequence is an increase in the threshold gain g. Given that gains are limited, it may be impossible to achieve lasing if the misalignment is too severe.

External cavity lasers may also be constructed by combining a SOA with a grating. There are two common configurations: Littrow and Littman. Each

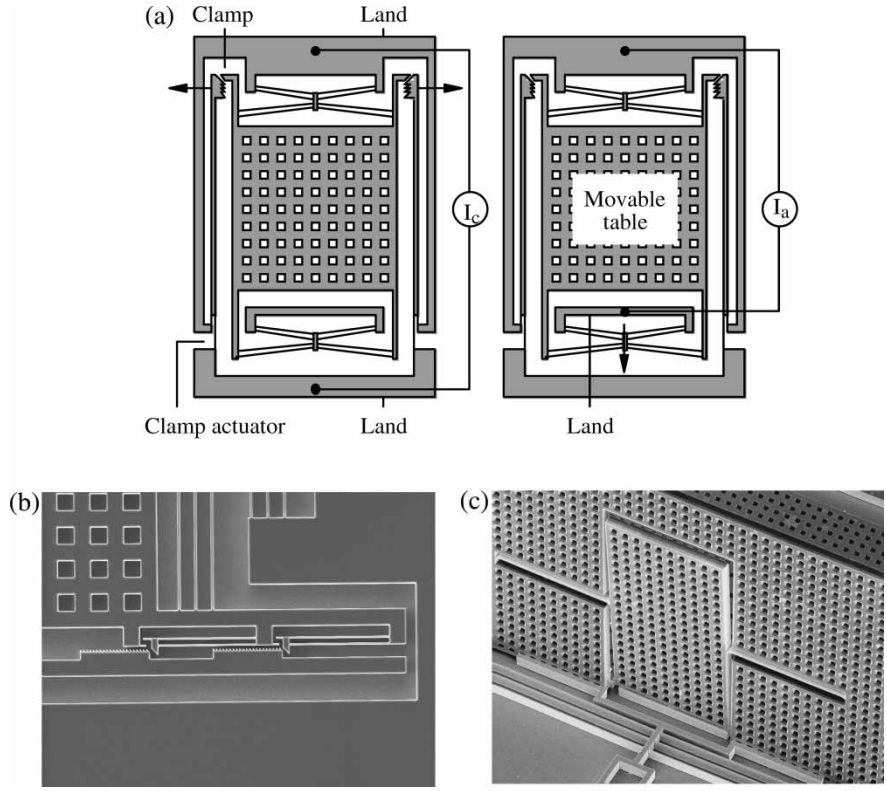

Fig. 13 (a) Latching alignment stage; (b) vernier latch, and (c) plug-assembled tilt mirror

consists of a HR/AR coated SOA, a collimating lens, and feedback elements. In the former case, shown in Fig. 12(b), reflection from a blazed grating is used, and the wavelength is tuned by rotating the grating. Mode-hop free tuning is achieved if the rotation centre is suitably located. Longitudinal resonance occurs when $\lambda = 2L_C/m$, where L_C is the effective cavity length and m is an integer. Comparison with the condition for grating retroreflection shows that L_C should be adjusted so that $L_C = m\Lambda \sin(\theta)$, and hence that $dL_C/d\theta = L_C/\tan(\theta)$. To first order, this can be achieved by mounting the grating on a radius arm extending tangentially from the grating, with a radius $R = L_C/\sin(\theta)$. Figure 12(b) shows a tuning element for a Littrow cavity based on a compound flexure that allows independent rotation and translation of the grating using two electrostatic actuators [**77**]. The completed element is shown in Fig. 1(c).

12 CONCLUSIONS

In the current paper, the arguments that control the fundamental design of optical MEMS have been presented. The use of an optimum Gaussian beam leads quickly to a set of standard arrangements of fibres, lenses, mirrors, and filters, for which alignment tolerances and scaling laws may be derived. The tolerances are generally so tight that very precise alignment is required, which leads to a requirement for an accurate manufacturing method such as MEMS technology. MEMS can also provide methods of moving optical surfaces to allow switching and tunable filtering, albeit on time-scales of milliseconds. However, the quality of any optical surfaces is important. Single crystal silicon has therefore provided the optimum solution for most applications.

In the past, accurate passive alignment was achieved using kinematic mounts, often combined with a retaining spring. More complex mounting systems are now being developed. Figure 13(a) shows an example of a linear translation stage, with electrothermal drives to control motion and a rack-and tooth latch to fix the stage in position [**46**]. Figure 13(b) shows a multi-section latch based on the Vernier principle, and Fig. 13(c) shows an elastic mount for a torsion mirror, held in a frame perpendicular to the stage. Such developments offer the possibility of low-cost packaging based on on-chip actuators for one-time assembly.

ACKNOWLEDGEMENTS

The author is grateful to those with whom he has worked at Imperial College on optical MEMS, including Dr A. Lohmann, Dr J. Stagg, and Dr H. Veladi, and

to external collaborators Professor D. Uttamchandani of Strathclyde University and the late Dr D. F. Moore of Cambridge University.

REFERENCES

1 **Muller, R. S.** and **Lau, Y. K.** Surface micromachined microoptical elements and systems. *Proc. IEEE*, 1998, **86**, 1705–1720.
2 **Walker, J. A.** The future of MEMS in telecommunications networks. *J. Micromech. Microeng.*, 2000, **10**, R1–R7.
3 **Syms, R. R. A.** and **Moore, D. F.** Optical MEMS for telecommunications. *Mater. Today*, 2002, (July/August Issue), 26–35.
4 **Wu, M. C., Solgaard, O.,** and **Ford, J. E.** Optical MEMS for lightwave communication. *J. Lightwave Technol.*, 2006, **24**, 4433–4454.
5 **Kogelnik, H.** and **Li, T.** Laser beams and resonators. *Appl. Opt.*, 1996, **5**, 1550–1567.
6 **Marcuse, D.** *Light transmission optics*, 1972, (Van Nostrand Reinhold, New York).
7 **Syms, R. R. A** Scaling laws for MEMS mirror rotation optical cross-connect switches. *IEEE J. Lightwave Technol.*, 2002, **20**, 1084–1094.
8 **Kovacs, G. T. A, Maluf, N. I.,** and **Petersen, K. E.** Bulk micromachining of silicon. *Proc. IEEE*, 1998, **86**, 1536–1551.
9 **Bustillo, J. M., Howe, R. T.,** and **Muller, R. S.** Surface micromachining for microelectro-mechanical systems. *Proc. IEEE*, 1998, **86**, 1552–1573.
10 **Gerner, M., Paatzsch, T., Weber, L., Schift, H., Smaglinski, I., Bauer, H.-D., Abraham, M.,** and **Ehrfeld, W.** Micro-optical components for fibre and integrated optics realised by the LIGA technique. In Proceedings of IEEE Workshop on Micro-Electro-Mechanical Systems, MEMS'95, Amsterdam, 29 January–2 February, 1995, pp. 328–333.
11 **Klaassen, E. H., Petersen, K., Noworolski, J. M., Logan, J., Maluf, N. I., Brown, J., Storment, C., McCulley, W.,** and **Kovacs, T. A.** Silicon fusion bonding and deep reactive ion etching: a new technology for microstructures. *Sens. Actuators*, 1996, **A52**, 132–139.
12 **Wu, M. C., Lin, L.-Y., Lee, S.-S.,** and **Pister, K. S. J.** Micromachined free-space integrated micro-optics. *Sens. Actuators*, 1995, **A50**, 127–134.
13 **Schroeder, C. M.** Accurate silicon spacer chips for an optical fiber cable connector. *Bell Syst. Tech. J.*, 1977, **57**, 91–97.
14 **Chang, P. C., Sriram, S.,** and **Wey, A. C.** Multiple fiber interconnect using silicon V-grooves. *Proc. SPIE*, 1987, **836**, 311–318.
15 **Hillerich, B.** and **Geyer, A.** Self-aligned flat-pack fibre-photodiode coupling. *Electron. Lett.*, 1988, **24**, 918–919.
16 **Parker, J. W., Harrison, P. M., Ayliffe, P. J., Clapp, T. V., Geear, M. C.,** and **Peall, R. G.** 6×700 MBIT/S array transmitter receiver pair realised in optohybrid silicon motherboard technology. *Microelectron. Eng.*, 1992, **19**, 215–218.
17 **Hashimoto, T., Nakasuga, Y., Yamada, Y., Terui, H., Yanagisawa, M., Akahori, Y., Tohmori, Y., Kato, K.,** and **Suzuki, Y.** Multichip optical hybrid integration technique with planar lightwave circuit platform. *IEEE, J. Lightwave Technol.*, 1998, **16**, 1249–1258.
18 **Tomlinson, W. J.** Applications of GRIN-rod lenses in optical fibre communication systems. *Appl. Opt.*, 1980, **19**, 1127–11138.
19 **Nicia, A.** Lens coupling in fiber-optic devices: efficiency limits. *Appl. Opt.*, 1981, **20**, 3136–3145.
20 **Wu, G., Mirza, A. R., Gamage, S. K., Ukrainczyk, L., Shashidar, N., Wruck, G.,** and **Ruda, M.** Design and use of compact lensed fibers for low cost packaging of optical MEMS. *J. Micromech. Microeng.*, 2004, **14**, 1367–1375.
21 **Hanafusa, H., Horiguchi, M.,** and **Noda, J.** Thermally-diffused expanded core fibers for low-loss and inexpensive photonic components. *Electron. Lett.*, 1991, **27**, 1968–1969.
22 **Tsai, R.-Y., Chang, C. S., Chu, C. W., Chen, T., Dai, F., Lin, D., Yan, S.,** and **Chang, A.** Thermally stable narrow bandpass filter prepared by reactive ion assisted sputtering. *Appl. Opt.*, 2001, **40**, 1593–1598.
23 **Daly, D., Stephens, R. F., Hutley, M. C.,** and **Davies, N.** The manufacture of lenses by melting photoresist. *Meas. Sci. Technol.*, 1990, **1**, 759–766.
24 **Lin, L. Y., Lee, S. S., Pister, K. S. J,** and **Wu, M. C.** Three-dimensional micro-Fresnel optical elements fabricated by micromachining techniques. *Electron. Lett.*, 1994, **30**, 448–449.
25 **Rosengren, L., Smith, L.,** and **Bäcklund, Y.** Micromachined optical planes and reflectors in silicon. *Sens. Actuators*, 1994, **A41–42**, 330–333.
26 **Klumpp, A., Kühl, K., Schaber, U., Käufl, H. U.,** and **Lang, W.** Anisotropic etching for optical gratings. *Sens. Actuators*, 1995, **A51**, 77–80.
27 **Cox, J. A., Zook, J. D., Ohnstein, T.,** and **Dobson, D. C.** Optical performance of high-aspect LIGA gratings. *Opt. Eng.*, 1997, **36**, 1367–1373.
28 **Lohmann, A.** and **Syms, R. R. A.** External cavity laser with a vertically-etched silicon blazed grating. *IEEE Photon. Technol. Lett.*, 2003, **15**, 120–122.
29 **Degani, O., Socher, E., Lipson, A., Leitner, T., Setter, D. J., Kaldor, S.,** and **Nemirovsky, Y.** Pull-in study of an electrostatic torsion microactuator. *J. Microelectromech. Syst.*, 1998, **7**, 373–379.
30 **Tang, W. C., Nguyen, T.-C. H.,** and **Howe, R. T.** Laterally driven polysilicon resonant microstructures. *Sens. Actuators*, 1989, **20**, 25–32.
31 **Selvakumar, A.** and **Najafi, K.** Vertical comb array microactuators. *IEEE/ASME J. Microelectromech. Syst.*, 2003, **12**, 440–449.
32 **Othman, M. B.** and **Brunnschweiler, A.** Electrothermally excited silicon beam mechanical resonators. *Electron. Lett.*, 1987, **23**, 728–730.
33 **Sehr, H., Evans, A. G. R., Brunnschweiler, A., Ensell, G. J.,** and **Niblock, T. E. G.** Fabrication and test of thermal vertical bimorph actuators for movement in the wafer plane. *J. Micromech. Microeng.*, 2001, **11**, 306–310.
34 **Guckel, H., Klein, J., Christenson, T., Skrobis, K., Laudon, M.,** and **Lovell, E. G.** Thermo-magnetic metal

flexure actuators. In Proceedings of IEEE Solid-State Sensor and Actuator Workshop, Hilton Head, SC, 22–25 June 1992, pp. 73–75.

35 **Sinclair, M. J.** A high force low area MEMS thermal actuator. In Proceedings of the 7th Intersocial Conference on Thermal and Thermomechanical Phenomena, ITHERM 2000, Las Vegas, 23–26 May 2000, pp. 127–132.

36 **Que, L., Park, J.,** and **Gianchandani, Y. B.** Bent-beam electrothermal actuators-Part I: Single beam and cascaded devices. *IEEE/ASME, J. Microelectromech. Syst.*, 2001, **10**, 247–254.

37 **Lee, J. H., Lee, M. L., Jang, W. I., Choi, C. A.,** and **Joo, J. W.** Bi-stable planar polysilicon microactuators with shallow arch-shaped leaf springs. *Proc. SPIE*, 1999, **3876**, 274–279.

38 **Petersen, K. E.** Micromechanical light modulator array fabricated on silicon. *Appl. Phys. Lett.*, 1977, **31**, 521–523.

39 **Van Kessel, P. F., Hornbeck, L. J., Meier, R. E.,** and **Douglass, M. R.** A MEMS-based projection display. *Proc. IEEE*, 1998, **86**, 1687–1704.

40 **Bostock, R. M., Collier, J. D., Jansen, R.-J. E., Jones, R., Moore, D. F.,** and **Townsend, J. E.** Silicon nitride microclips for the kinematic location of optic fibres in silicon V-shaped grooves. *J. Micromech. Microeng.*, 1998, **8**, 343–360.

41 **Syms, R. R. A., Zou, H., Yao, J., Uttamchandani, D.,** and **Stagg, J.** Scalable electrothermal MEMS actuator for optical fibre alignment. *J. Micromech. Microeng.*, 2004, **14**, 1633–1639.

42 **Unamuno, A., Yao, J.,** and **Uttamchandani, D.** Alignment and fixing of fibre optics based on electrothermal MEMS actuators. *IEEE Photon. Technol. Lett.*, 2005, **17**, 816–818.

43 **Haake, J. M., Wood, R. L.,** and **Duhler, V. R.** In-package active fiber optic micro-aligner. *Proc. SPIE*, 1998, **3276**, 207–219.

44 **Field, L. A., Burriesci, D. L., Robrisch, P. R.,** and **Ruby, R. C.** Micromachined 1×2 optical-fiber switch. *Sens. Actuators*, 1996, **A53**, 311–315.

45 **Kopka, P., Hoffmann, M.,** and **Voges, E.** Coupled U-shaped cantilever actuators for 1×4 and 2×2 optical fibre switches. *J. Micromech. Microeng.*, 2000, **10**, 260–264.

46 **Syms, R. R. A., Zou, H.,** and **Stagg, J.** MOEMS alignment stages with Vernier latch mechanisms. *J. Opt. A, Pure Appl. Opt.*, 2006, **8**, S305–S312.

47 **Marxer, C., Griss, P.,** and **de Rooij, N. F.** A variable optical attenuator based on silicon micromechanics. *IEEE Photon. Technol. Lett.*, 1999, **11**, 233–235.

48 **Wood, R., Dhuler, V.,** and **Hill, E.** A MEMS variable attenuator. In IEEE/LEOS International Conference on Optical MEMS, Kauai, Hawaii, 21–24 August 2000, pp. 121–122

49 **Li, L.** and **Uttamchandani, D.** Design and evaluation of a MEMS optical chopper for fibre optic applications. *IEE Proc. Sci. Meas. Technol.*, 2004, **151**, 67–75.

50 **Syms, R. R. A., Zou, H., Stagg, J.,** and **Veladi, H.** Sliding-blade MEMS iris and variable optical attenuator. *J. Micromech. Microeng.*, 2004, **14**, 1700–1710.

51 **Syms, R. R. A., Zou, H., Stagg, J.,** and **Moore, D. F.** Multi-state latching MEMS variable optical attenuator. *IEEE Photon. Technol. Lett.*, 2004, **16**, 191–193.

52 **Kim, C.-H., Park, N.,** and **Kim, Y.-K.** Development and characterization MEMS reflective type variable optical attenuator using off-axis misalignment. In IEEE/LEOS International Conference on Optical MEMS, Lugano, Switzerland, 20–23 August 2002, pp. 55–56.

53 **Sumriddetchkajorn, S.** and **Riza, N. A.** Fault-tolerant three-port fiber-optic attenuator using small tilt micromirror device. *Opt. Commun.*, 2002, **205**, 77–86.

54 **Marxer, C.** and **de Rooij, N. F.** Micro-opto-mechanical 2×2 switch for single-mode fibers based on a plasma-etched silicon mirror and electrostatic actuation. *IEEE J. Lightwave Technol*, 1999, **LT-17**, 2–6.

55 **Helin, P., Mita, M., Bourouina, T., Reyne, G.,** and **Fujita, H.** Self-aligned micromachining process for large-scale, free-space optical cross-connects. *IEEE, J. Lightwave Technol.*, 2000, **18**, 1785–1791.

56 **Toshiyoshi, H.** and **Fujita, H.** Electrostatic micro torsion mirrors for an optical switch matrix. *IEEE/ASME, J. Microelectromech. Syst.*, 1996, **5**, 231–237.

57 **Lin, L. Y., Goldstein, E. L., Simmona, J. M.,** and **Tkach, R. W.** Free-space micromachined optical switches with submillisecond switching time for large-scale optical crossconnects. *IEEE Photon. Technol. Lett.*, 1998, **10**, 525–527.

58 **Aksyuk, V., Barber, B., Giles, C. R., Ruel, R., Stulz, L.,** and **Bishop, D.** Low insertion loss packaged and fibre connectorised MEMS reflective optical switch. *Electron. Lett.*, 1998, **34**, 1413–1414.

59 **Laor, H.** Construction and performance of a 576×576 single-stage OXC. In Proceedings of LEOS'99, San Francisco, CA, 8–11 November 1999, vol. 2, pp. 481–482.

60 **Lee, S. S., Huang, L.-S., Kim, C.-J.,** and **Wu, M. C.** Free-space fiber-optic switches based on MEMS vertical torsion mirrors. *J. Lightwave Technol.*, 1999, **17**, 7–13.

61 **Aksyuk, V. A., Pardo, F., Bolle, C. A., Arney, S. C., Giles, C. R.,** and **Bishop, D. J.** Lucent Microstar micromirror array technology for large optical crossconnects. *Proc. SPIE*, 2000, **4178**, 320–324.

62 **Greywall, D. S., Busch, P. A., Pardo, F., Carr, D. W., Bogart, G.,** and **Soh, H. T.** Crystalline silicon tilting mirrors for optical cross-connect switches. *IEEE/ASME, J. Microelectromech. Syst.*, 2003, **12**, 708–712.

63 **Sawada, R., Yamaguchi, J., Higurashi, E., Shimazu, A., Yamamoto, T., Takeuchi, N.,** and **Uenishi, Y.** Single Si crystal 1024 ch MEMS miirror based on terraced electrodes and high-aspect ratio torsion spring for 3-D cross-connect switch. In IEEE/LEOS International Conference on Optical MEMS, Lugano, Switzerland, 20–23 August 2002, Paper TuB1.

64 **Hah, D., Huang, S. T., Tsai, J., Toshiyoshi, H.,** and **Wu, M. C.** Low-voltage large scan angle MEMS analog micromirror arrays with hidden vertical comb-drive actuators. *IEEE/ASME, J. Microelectromech. Syst.*, 2004, **13**, 279–289.

65 **Yano, M., Yamagishi, F.,** and **Tsuda, T.** Optical MEMS for photonic switching – compact and stable optical crossconnect switches for simple, fast and flexible application in recent photonic networks. *IEEE, J. Sel. Top. Quant. Electron.*, 2005, **11**, 383–394.

66 **Ford, J. E., Aksyuk, V. A., Bishop, D. J.,** and **Walker, J. A.** Wavelength add-drop switching using tilting micromirrors. *IEEE J. Lightwave Technol.*, 1999, **17**, 904–911.

67 **Bernstein, J. J., Dokmeci, M. R., Kirkos, G., Osenar, A. B., Peanasky, J.,** and **Pareek, A.** MEMS tilt-mirror spatial light modulator for a dynamic spectral equalizer. *IEEE/ASME, J. Microelectromech. Syst.*, 2004, **13**, 272–278

68 **Kaman, V., Zheng, X., Helkey, R. J., Pusarla, C.,** and **Bowers, J. E.** A 32-element 8-bit photonic true-time-delay system based on a 288 × 288 3-D MEMS optical switch. *IEEE Photon. Technol. Lett.*, 2003, **15**, 849–851.

69 **Mallinson, S. R.** and **Jerman, J. H.** Miniature micromachined Fabry–Perot interferometers in silicon. *Electron. Lett.*, 1987, **23**, 1041–1043.

70 **Tran, A. T. T. D., Lo, Y. H., Zhu, Z. Q., Haronian, D.,** and **Mzdy, E.** Surface micromachined Fabry Perot tunable filter. *IEEE Photon. Technol. Lett.*, 1996, **8**, 393–395.

71 **Ford, J. E., Walker, J. A.,** and **Goossen, K. W.** Optical fiber-coupled variable attenuator using a MARS modulator. *Proc. SPIE*, 1997, **3226**, 86–93.

72 **Luo, C.** and **Goossen, K. W.** Optical microelectromechanical system array for free-space retrocommunication. *IEEE Photon. Technol. Lett.*, 2004, **16**, 2045–2047.

73 **Lipson, A.** and **Yeatman, E. M.** Low loss 1D photonic band gap filter in (110) silicon. *Opt. Lett.*, 2006, **31**, 395–397.

74 **Larson, M. C.** and **Harris, J. S.** Wide and continuously tunable vertical cavity surface emitting lasers using a micromachined deformable-membrane mirror. *Appl. Phys. Lett.*, 1996, **68**, 891–893.

75 **Li, M. Y., Li, G. S.,** and **Chang-Hasnain, C. J.** Top-emitting micromechanical VCSEL with a 31.6 nm tuning range. *IEEE Photon. Technol. Lett.*, 1998, **10**, 18–20.

76 **Uenishi, Y., Tsugai, M.,** and **Mehregany, M.** Hybrid-integrated laser diode micro-external mirror fabricated by (110) silicon micromachining. *Electron. Lett.*, 1995, **31**, 965–966.

77 **Syms, R. R. A.** and **Lohmann, A.** MOEMS tuning element for a Littrow external cavity laser. *IEEE/ASME, J. Microelectromech. Syst.*, 2003, **12**, 921–928.

78 **Zhang, X. M., Liu, A. Q., Lu, C.,** and **Tang, D. Y.** Continuous wavelength tuning in micro-machined Littrow external-cavity lasers. *IEEE J. Quant. Electron.*, 2005, **41**, 187–197.

79 **Berger, J. D., Zhang, Y., Grade, J. D., Lee, H., Hrinya, S.,** and **Jerman, J. H.** Widely tunable external cavity diode laser based on a MEMS electrostatic rotary actuator. In OFC 2001, Anaheim, CA, 17–22 March 2001, Paper Tuj2.

80 **Abramowitz, M.** and **Stegun, I. A.** *Handbook of mathematical functions*, 1965, (Dover Publications, New York).